Ultrasound in Medicine & Biology 000 (2024) 1–11

Contents lists available at ScienceDirect

Ultrasound in Medicine & Biology

journal homepage: www.elsevier.com/locate/ultrasmedbio

Original Contribution

Amplitude-Modulation Frequency Optimization for Enhancing Harmonic Motion Imaging Performance of Breast Tumors in the Clinic

Yangpei Liu [a], Md Murad Hossain [a], Xiaoyue Judy Li [a], Elisa E. Konofagou [a,b,c,*]

[a] Department of Biomedical Engineering, Columbia University, New York, NY, USA
[b] Department of Radiology, Columbia University Irving Medical Center, New York, NY, USA
[c] Department of Neurological Surgery, Columbia University Irving Medical Center, New York, NY, USA

ARTICLE INFO

Keywords:
Amplitude modulation frequency
Breast tumor
Elastography
Focused ultrasound
Harmonic motion imaging
Neoadjuvant chemotherapy

ABSTRACT

Objective: Elastography images tissue mechanical responses and infers the underlying properties to aid diagnosis and treatment response monitoring. The estimation of absolute or relative tumor properties may vary with dimensions even when the mechanical properties remain constant. Harmonic motion imaging (HMI) uses amplitude-modulated (AM) focused ultrasound to interrogate the targeted tissue's viscoelastic properties. In this study, effects of AM frequencies on HMI were investigated in terms of inclusion relative stiffness and size estimation.
Methods: AM frequencies from 200 to 600 Hz in steps of 100 Hz were considered using a 5.3-kPa phantom with cylindrical inclusions (Young's modulus: 22, 31, 44, 56 kPa, and diameter: 4.8, 8.1, 13.6, 19.8 mm) to optimize the performance of HMI in characterizing tumors with the same mechanical properties and of different dimensions.
Results: Consistent displacement ratios (DRs) (17.5% variation) of the inclusion to background were obtained with 200-Hz AM for breast-tumor-mimicking inclusions albeit a suboptimal inclusion size estimation obtained. 400-Hz was otherwise used for small and low-contrast inclusions (4.8 mm, 22 or 31 kPa). A linear relationship ($R^2 = 0.9043$) was found between the inverse DR at these frequencies and the Young's modulus ratio. 400 Hz obtained the most accurate inclusion size estimation with an overall estimation error on the lateral dimension of 0.5 mm. *In vivo* imaging of breast cancer patients ($n = 5$) was performed at 200 or 400 Hz.
Conclusion: The results presented herein indicate that the HMI AM frequency could be optimized adaptively in cases of different applications, i.e., at 200 or 400 Hz, depending on whether aimed for consistent DR measurement for tumor response assessment or tumor margin delineation for surgical planning. HMI may thus be capable of predicting the pathologic endpoint of tumors in response to neoadjuvant chemotherapy (NACT) as early as 3 weeks into treatment.

Introduction

Breast cancer accounted for 31% of newly diagnosed female cancers in 2023 and the second leading cause of cancer-related mortality in the United States [1]. Neoadjuvant treatment may be considered, aiming to downstage tumors before surgical interventions and guide adjuvant treatments. Mammography [2,3], ultrasound [2–6], and magnetic resonance imaging (MRI) [7–9] have been employed to monitor tumor response to treatment and predicting pathologic end points based on the changes in tumor volumes or mechanical properties. Results indicated that responsive tumors had at least a 50% decrease in volume [3,9] and 20%–60% decrease in stiffness [4,6]. Ultrasound, requiring no contrast agents, being nonionizing and cost-effective, proves well-suited for repetitive tumor imaging.

Over the past few decades, ultrasound elastography [10] has been extensively studied to estimate stiffness of the liver [11], prostate [12,13], pancreas [14], and breast [15–17] quantitatively or qualitatively. Among these techniques, acoustic radiation force-based methods, e.g., Acoustic Radiation Force Impulse (ARFI) imaging [18], Harmonic Motion Imaging (HMI) [19,20], Viscoelastic Response (VisR) ultrasound imaging [21], and Shear Wave Elasticity Imaging (SWEI) [22,23], demand less training in comparison to alternative methods that require an external compression with the transducer [24], and are thus expected to be less prone to interoperator variability. On the other hand, although shear wave-based methods provide quantitative measurements of tissue stiffness by estimating off-axis shear wave speeds, they can suffer from wave distortion due to tissue heterogeneity [25–27] and a reduction in spatial resolution due to wave speed estimation over a lateral window of several millimeters in length. On-axis displacement-based methods are less limited in cases of deep-seated masses at high stiffnesses because tissue displacements exhibit the highest amplitude in the region of excitation and are lower off-axis due to attenuation and viscous losses. However, they usually provide qualitative measurements of tissue mechanical properties. In HMI, the intensity of focused ultrasound (FUS) is modulated

* Corresponding author. Columbia University Medical Center, 630 West 168th Street, Physicians & Surgeons 19-418, New York, NY 10032, USA
E-mail address: ek2191@columbia.edu (E.E. Konofagou).

https://doi.org/10.1016/j.ultrasmedbio.2024.09.021
Received 27 June 2024; Revised 26 September 2024; Accepted 29 September 2024

Please cite this article as: Y. Liu et al., Amplitude-Modulation Frequency Optimization for Enhancing Harmonic Motion Imaging Performance of Breast Tumors in the Clinic, Ultrasound in Medicine & Biology (2024), https://doi.org/10.1016/j.ultrasmedbio.2024.09.021

[28] to exert oscillatory acoustic radiation force on the tissue. The resulting "on-axis" tissue response is tracked synchronously using an imaging array aligned coaxially. Sinusoidal tissue displacements are then estimated to provide insights on the stiffness of underlying tissues, with lower displacements observed in stiffer tissues. Advantages of HMI over other techniques involve: (1) the utilization of FUS enabling deep tissue characterization and (2) in-plane bulk motion artifacts being easily filtered from the distinct amplitude modulation (AM) frequency [29]. Previous studies from our group have demonstrated applications of HMI in pancreatic and breast tumor characterization, tumor response assessment to chemotherapy in *in vivo* murine models [17,30,31], *ex vivo* human specimens [32–34], and *in vivo* clinical patients [31,35].

Ideally, stiffness parameters estimated in HMI or other elastography techniques characterize the tissue mechanical properties accurately regardless of geometries or dimensions. However, as demonstrated by Hossain et al. [36] and Saharkhiz et al. [37] in HMI, and Denis et al. [38] in shear wave elastography, inclusion dimensions significantly affected the stiffness measurement. For the same actual stiffness, larger inclusions appeared to be stiffer, and vice versa [4,36]. This presumably undermines the accuracy and specificity of ultrasound elastography in tumor characterization and treatment response assessment. To address this, Gu et al. [4] introduced a new parameter in SWEI, mass characteristic frequency, f_{mass}, by dividing the averaged tumor shear wave speed by its largest dimension measured on the B-mode. It was shown that f_{mass} was able to predict pathologic end points for breast cancer patients, albeit at a later time-point. Saharkhiz et al. [37] have investigated the effects of AM frequencies on HMI-derived inclusion contrast and contrast-to-noise ratio (CNR), suggesting high AM frequencies (200 to 500 Hz) when characterizing small inclusions <6 mm. There remains, however, a clinical need to reduce the inconsistency in HMI-derived relative stiffness of inclusions with the same modulus but different dimensions. Besides, the accuracy of HMI inclusion size estimation is pending evaluation, which potentially provides insights to guide surgical excision.

Another limitation in HMI and other elastography techniques is that mechanical movement of the transducers using a stepper motor [12,13,39] to cover the entire region of interest (ROI) is required when characterizing large masses. Extended data acquisition time inevitably complicates postprocessing, introducing more artifacts due to patient motion. In some cases, registration between scans based on radiofrequency (RF) cross-correlation was feasible [35]. Nevertheless, expediting data acquisition is of greater significance in clinical settings. Electronic beam steering using a multielement FUS transducer and plane wave imaging reduced the amount of mechanical movements and shortened HMI data acquisition by a factor of fivefold [39], at the cost of a slight decrease in the image qualities [40]. Enabling focused tracking and simultaneous beam steering of the FUS excitation will preserve the desired image qualities.

Therefore, this study investigated AM frequencies in HMI using an elastic phantom with inclusions of varying diameters and Young's moduli ($n = 16$). The aim was to optimize the performance of HMI in imaging tumors of different dimensions with the same mechanical properties. First, we conducted a comprehensive comparison to minimize variations in DR measurements of inclusions with the same mechanical property but of different sizes. Second, inclusion size estimation based on HMI maps was evaluated, and the AM frequency that obtained the most accurate inclusion size estimation was identified. Applications of the optimized AM frequencies were demonstrated in *in vivo* breast cancer patients ($n = 5$) with the purpose of early prediction of tumor response to neoadjuvant chemotherapy (NACT, $n = 4$).

Materials and methods

HMI system and pulse sequence

Figure 1a (left) shows the schematic of HMI data acquisition [40]. The 256-channel Vantage research platform with HIFU options (Vantage 256, Verasonics Inc., Kirkland, WA, USA) was connected to an external DC power supply (QPX 600DP, Aim-TTi Ltd., Huntingdon, Cambs., UK) to drive the annular 128-element FUS transducer (4.5 MHz, geometric focus: 76 mm, axial x lateral focal spot: 4.30 × 0. 39 mm, H265, Sonic Concepts Inc., Bothell, WA, USA). The remaining 128 channels drove the 104-element imaging array (7.8 MHz, P12-5, ATL Phillips, Bothell, WA, USA) coaligned through the FUS central opening to track the tissue response. The transducer assembly was attached with a coupling cone filled with degassed deionized water. The robotic arm (UR5e, Universal Robots USA, Inc., Garden City, NY, USA) was used to position and then translate the transducers laterally in a 1D raster scanning format, the step size of which was 1.8 or 3.2 mm depending on the FUS electronic beam steering range. To complete a 21-point HMI scan covering a lateral range of 37.8 or 67.2 mm, the data acquisition time was 80 or 95 s.

The HMI pulse sequence (Fig. 1b) consisted of amplitude-modulated excitation pulses (red) interleaved with pulse-echo imaging pulses (blue) [39]. The FUS excitation duty cycle of 22.6% was optimized with the external power supply to produce an *in-situ* peak-negative pressure of 3.9 MPa. The idle time between consecutive excitation and imaging pulses was 90 μs to avoid strong FUS interference with imaging [40]. Conventionally, the excitation modulating wave consisted of a single frequency (Fig. 1b, left). Hossain et al. [36] recently have introduced a novel modulation sequence using a linear combination of multiple frequencies, termed "multi-AM." Figure 1b (right) demonstrates a multi-AM sequence of 200 and 400 Hz, $\cos(2\pi * 200t) + 2\cos(2\pi * 400t)$. For both single- and multi-AM sequences in this study, the excitation duration at each scan point was 30 ms, i.e., 6 cycles [31] for a 200-Hz sequence. The imaging sequence consisted of focused tracking using a transmit (Tx) F-number of 4.1 and parallel tracking in receive (Rx F/2.6, i.e., the entire aperture) as described in [40]. The FUS pulse repetition frequency (PRF) and imaging frame rate were 9x the AM frequency [37] in a single-AM sequence or 9x the highest in a multi-AM sequence.

Electronic beam steering

By controlling each element of the 128-element FUS transducer individually, the coaxially aligned FUS excitation and focused tracking beam were simultaneously steered electronically in this study. The beam steering range was optimized according to the applied AM frequency. As discussed in [37], the amplitude of HMI displacements decreases with increased AM frequencies, partially due to the increased viscosity [41] and inertia [21] effects. Meanwhile, drops of acoustic pressures were measured with beam steering further away from the geometric focus [39]. Therefore, to maintain tissue displacements above the system sensitivity, the lateral beam steering range spanned from -1.2 to 1.2 mm in a step size of 0.8 mm for low AM frequencies (200 and 300 Hz), and from -0.6 to 0.6 mm in a step size of 0.6 mm for high AM frequencies (400 to 600 Hz, considering the maximum applied AM frequency in a multi-AM sequence). The axial steering range spanned from -4 to 4 mm in a step size of 4 mm for all cases. Similar to mechanical steering, at each electronically steered point, a single-point HMI was performed.

Phantom experiment

The performance of HMI in imaging elastic inclusions at AM frequencies from 200 to 600 Hz in a step size of 100 Hz was assessed. Sixteen stepped-cylindrical inclusions with clinical breast-tumor-mimicking properties [4,16,38,42] (diameter: 4.8, 8.1, 13.6, and 19.8 mm, Young's modulus: 22, 31, 44, and 56 kPa, background: 5.3 kPa, custom model, CIRS Inc., Norfolk, VA, USA) were imaged. The inclusion diameters reported here were measured on the B-mode images acquired during HMI data acquisition (observer: YL), and Young's moduli were provided by the manufacturer. Four independent HMI scans were acquired at varying elevational locations, not necessarily the center, with the same cross-sectional diameter for each inclusion. In addition, the multi-AM

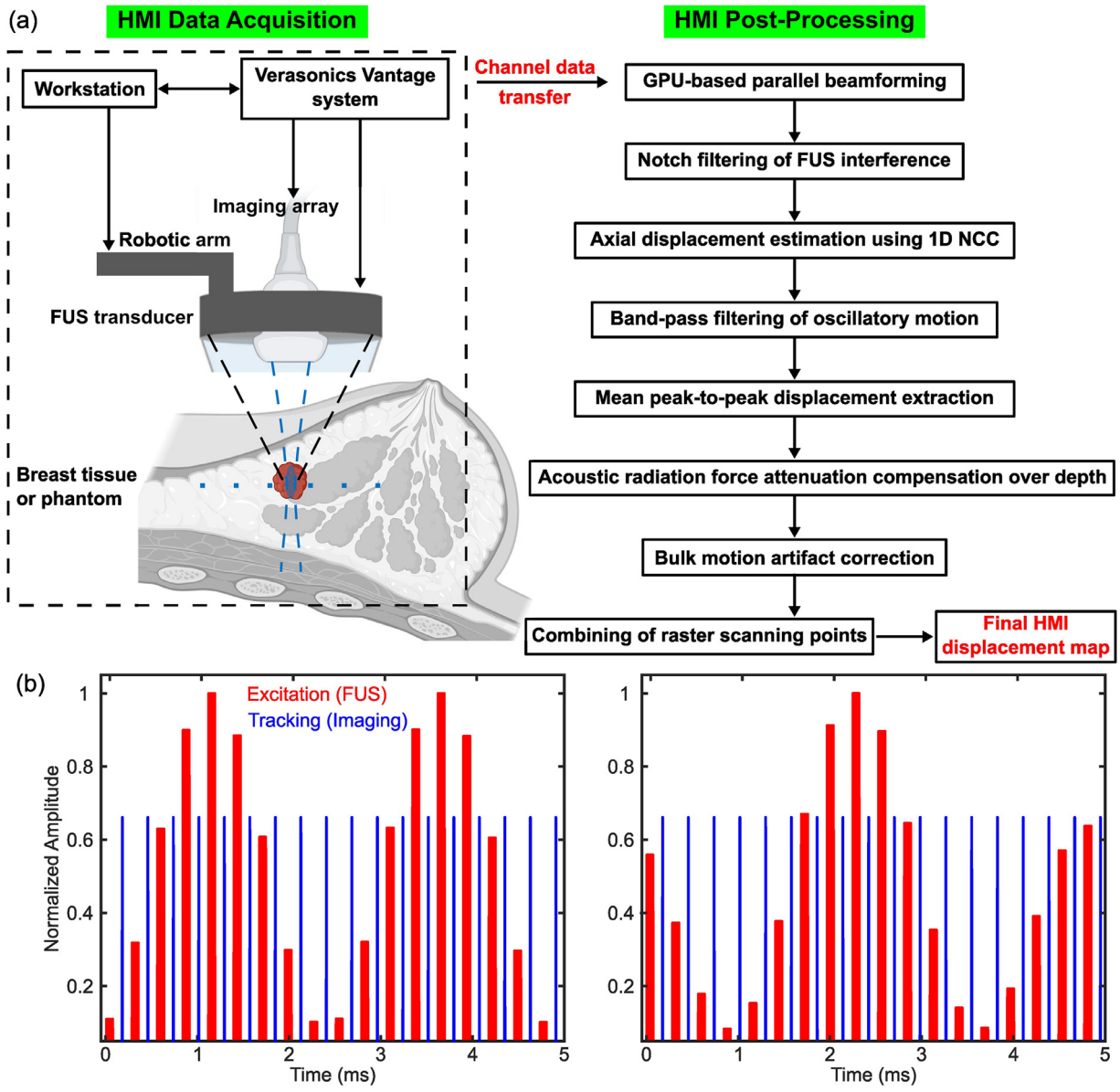

Figure 1. Schematic of the HMI experimental setup, data processing, and the interleaved pulse sequences. (a) Left: A 256-channel Verasonics research system controlling both the FUS transducer and the imaging array. The FUS focal spot and the imaging plane were coaligned. 1D HMI raster scanning was realized using a robotic arm. Right: Channel data were transferred from the Verasonics workstation to a local PC for postprocessing. (b) HMI pulse sequences of single (400 Hz, left) and multiple AM frequencies (200 and 400 Hz, right). FUS excitation pulses (red) were interleaved with imaging pulses (blue). The FUS pulse repetition frequency and imaging frame rate were 9x the maximum applied AM frequency, i.e., 3600 Hz for 400 Hz AM.

sequence, consisting of 200 and 400 Hz, was tested and compared to the single-AM sequences. The multi-AM weights [36] were determined empirically to produce comparable amplitudes of interframe displacements at both AM frequencies [37] (Fig. 4a).

In vivo *clinical breast tumor imaging*

Clinical performance of the optimized AM frequency and the multi-AM sequence were demonstrated in female patients ($n = 5$) diagnosed with high-grade ductal carcinoma *in situ* (DCIS, $n = 1$), invasive ductal carcinoma (IDC, $n = 3$), or fibroadenoma ($n = 1$). Patient information is summarized in Table 1. The imaging procedures followed the protocol approved by the institutional review board (IRB) of Columbia University (protocol#: AAAT4412). Informed written consent was obtained from all participants following consultation with their treating physicians. Clinical B-mode images acquired at diagnosis were retrieved from the hospital to aid tumor localization. Before each HMI scan, a handheld ultrasound scanner (Butterfly iQ, Butterfly Network Inc., Guilford, CT, USA) was used to localize the tumor (observer: XJL) with the patient lying supine. Given the time constraints for *in vivo* scans, only HMI using the optimized AM frequency (200 Hz), based on results from the phantom study, was performed for Patients 1–4. For Patient 5, who was imaged using the multi-AM sequence, $\cos(2\pi * 200t) + 2\cos(2\pi * 400t)$, both multi- and single-AM HMI were performed for comparisons: one multi-AM scan and two single-AM scans (200 and 400 Hz). For Patients 1–4, HMI scans were performed at two different time-points during their NACT treatment: (1) baseline before treatment and (2) early follow-up at 3 weeks into treatment. Due to technical difficulties, baseline HMI scans of Patient 1 were discarded.

HMI data processing

As described in Figure 1a (right), channel data sampled at 31.25 MHz and stored on the Verasonics workstation were transferred to a local

Table 1
Patient Characteristics

	Patient 1	Patient 2	Patient 3	Patient 4	Patient 5
Age	62	53	57	53	47
Tumor size	2.5 cm	3.0 cm	1.1 cm	2.6 cm	1.0 cm
Diagnosis	DCIS	IDC	IDC	IDC	Fibroadenoma
Molecular subtype	ER-, PR-, HER2 +	ER + , PR-, HER2 +	ER-, PR-, HER2-	ER + , PR + , HER2-	ER + , PR + , HER2-
Neoadjuvant therapy	Pertuzumab, Trastuzumab-Anns, Docetaxel	Docetaxel, Carboplatin, Pertuzumab, Trastuzumab-Anns	Carboplatin, Paclitaxel, Pembrolizumab, Cyclophosphamide, Doxorubicin	Paclitaxel, Doxorubicin, Cyclophosphamide	/
Pathologic endpoints	Noncomplete response	Complete response	Noncomplete response	/	/

computer for offline processing (MATLAB R2019b, MathWorks, Natick, MA, USA). For each raster scan, a GPU-accelerated delay-and-sum algorithm was applied to reconstruct the beamformed RF lines. Residual FUS interference with the imaging bandwidth (5 to 12 MHz) was filtered using second-order Butterworth notch filters at the fundamental (4.5 MHz) and 2nd harmonic (9 MHz) of the FUS. 1D normalized cross-correlation (NCC) [43] with cosine interpolation [44] was then implemented to estimate the interframe axial displacements using a 4-λ window and 95% overlap [40]. Displacement estimation with a cross-correlation coefficient lower than 0.99 was rejected and median-interpolated. For the multi-AM sequence, interframe displacements at each AM frequency were calculated between frames with the same phase shift in the corresponding AM cycle to account for the effect of different numbers of samples per AM cycle. For example, when the tracking frame rate was 3600 Hz, displacements at 400 Hz were estimated between consecutive frames (frames k and k + 1), whereas displacements at 200 Hz were estimated between alternate frames (frames k and k + 2, Fig. 4a). Following that, an 18th-order infinite impulse response (IIR) bandpass filter with Hamming windowing was designed to extract the sinusoidal displacements at each AM frequency. Last, peak-to-peak (P2P) displacements were averaged over cycles to produce a P2P displacement image around the FUS focus spanning 14 mm axially and 1.2 or 1.6 mm laterally for a lateral electronic beam steering step size of 0.6 or 0.8 mm to provide overlaps between raster scans.

Next, P2P displacement images from all raster scans were normalized over the axial range to compensate for the acoustic radiation force variation over depth. The normalization curve was calculated by averaging two raster scans in the background identified on the B-mode. Therefore, the final HMI displacement map was displayed as the displacement "ratio" with respect to the averaged background displacements. For *in vivo* clinical scans, breath holding was not practiced promoting patient comfort, and thus, bulk motion correction between raster scans was necessary. Three plane wave frames were obtained right before each HMI raster scan. 2D NCC between neighboring beamformed RF frames was performed using a 5 × 3 mm (axial x lateral) window and step sizes of 0.2 mm in both directions [35]. Offsets yielding the highest correlation coefficient were retrieved for motion correction. Finally, the normalized and registered raster scans were combined [40] to form the 2D HMI displacement map.

Inclusion stiffness biomarker and size estimation

Relative tissue stiffness can be retrieved from HMI maps using the displacement ratio (DR) [36] of inclusions or tumors to surrounding background or healthy tissues. As shown in Figure 2, the inclusion boundary was first delineated on the B-mode (observer: YL). For phantoms, one square inclusion ROI (red) with sides measuring 0.6x the inclusion diameter and two adjacent rectangle background ROIs (green) that make up identical areas at the same depth were drawn. For biological tissues, because of the irregular tumor boundary and limited field of view in the background, ROIs were drawn with areas not necessarily equal between tumors and surrounding healthy tissues (e.g., Fig. 8). Using those, mean normalized HMI displacements were calculated in the inclusion (μ_i) and background (μ_b), and the DR was defined as μ_i/μ_b. Therefore, a DR of 1 indicates a mechanically homogeneous region, and DRs below 1 are anticipated in stiff inclusions as they are displaced less compared to the background. The optimized AM frequency was expected to produce consistent DR measurements for inclusions with the same mechanical properties albeit different dimensions.

Inclusion size was estimated from the HMI displacement maps in phantoms and compared to the ground truth measured on the B-mode images. First, the 2D parametric HMI map was binarized using Otsu's method (*imbinarize* function in MATLAB, threshold: 0.15 quantile of the HMI map). Next, the inclusion boundaries were extracted using the *bwboundaries* function, and an ellipse was fit to the extracted boundaries using the least-squares criterion (*fit_ellipse* function [45]). As shown in Figure 6, the long and short axes of the fit ellipse were reported as axial and lateral diameters. The equivalent diameter, defined as the square root of the multiplication of axial and lateral diameters, was also reported.

Statistical analysis

Previously, HMI displacements were found to be inversely correlated with the elastic modulus [28]. Therefore, linear regression was performed between the inverse DR and Young's modulus ratio of the inclusion to background with each combination of AM frequencies. The regression slope, R^2, and root mean squared error (RMSE), as well as F-statistics of the mean squared errors (MSE) between linear fittings, were calculated in Prism 7 (GraphPad Software, La Jolla, CA, USA). 64 measurements (4 independent measurements for each inclusion configuration of 4 different diameters and 4 Young's moduli) were considered and a $p < 0.01$ was considered statistically significant.

Results

Inclusion DR

Figure 2 shows B-mode images and normalized HMI displacement maps of 22- and 56-kPa inclusions with 13.6- and 4.8-mm diameters. All obtained DRs were below 1, agreeing that the imaged inclusions were stiffer than the background (5.3 kPa). In addition, higher DRs, indicating lower HMI contrast, were obtained for the 22-kPa inclusions compared to the 56-kPa, despite a wide range of DRs measured for inclusions with the same Young's modulus while different diameters. For instance, at 300 Hz, 48.2% and 40.4% differences in measured DRs were observed for the 22-kPa inclusions with different diameters (DRs of 0.31 and 0.46) and the 56-kPa inclusions (DRs of 0.12 and 0.17), respectively. Moreover, at 400 Hz, a 71.9% difference was seen for the 56-kPa inclusions (DRs of 0.10 and 0.17).

Figure 3 summarizes inclusion DRs for 22-, 31-, 44-, and 56-kPa inclusions with 4.8-, 8.1-, 13.6-, and 19.8-mm diameters at different AM frequencies over four independent acquisitions. Four observations were notable. First, DRs overall decrease as the inclusion's Young's modulus

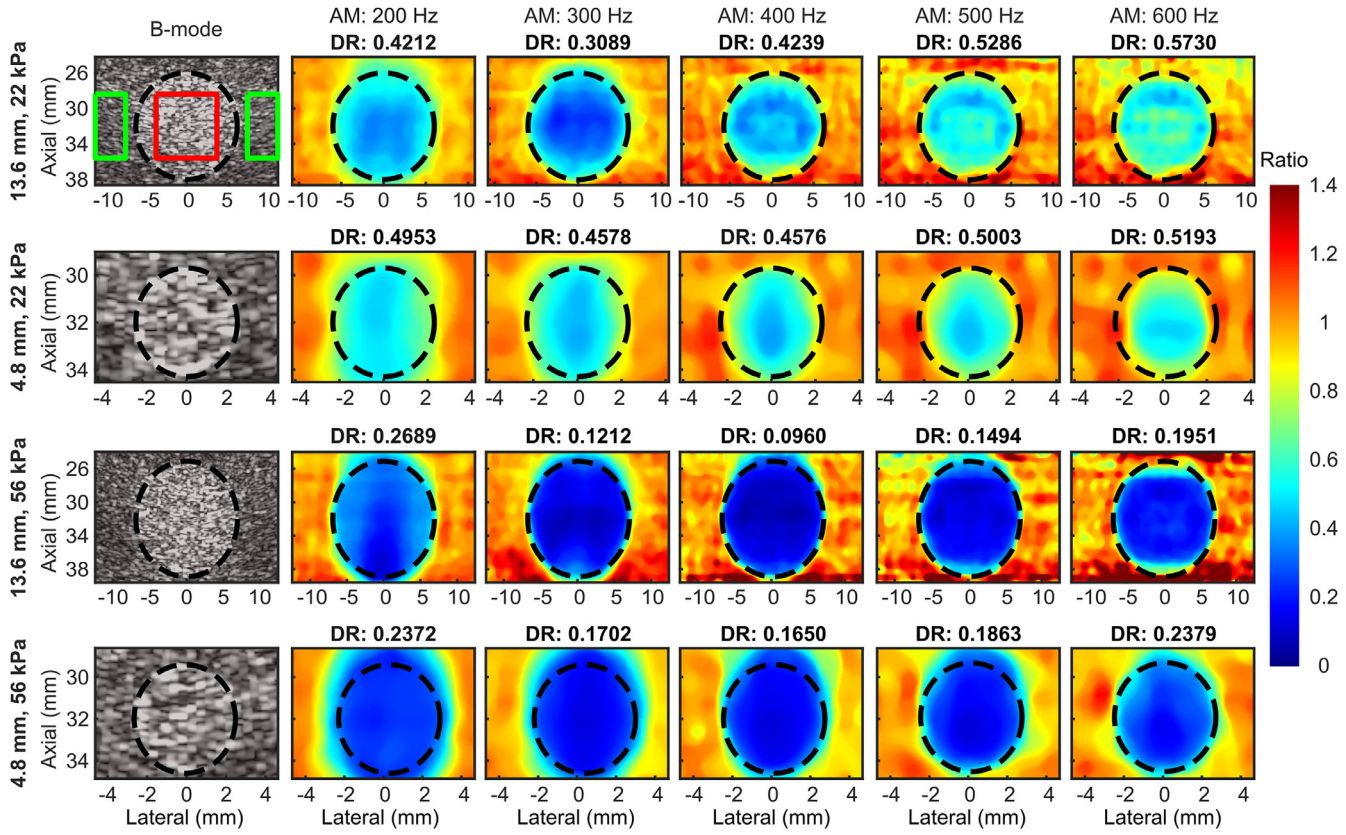

Figure 2. B-mode and normalized HMI maps at different AM frequencies of inclusions with (diameter, Young's modulus) of (1st row, 13.6 mm, 22 kPa), (2nd row, 4.8 mm, 22 kPa), (3rd row, 13.6 mm, 56 kPa), and (4th row, 4.8 mm, 56 kPa) embedded in a 5.3-kPa background. Dashed black, solid red, and green contours represent the inclusion boundaries derived from the B-mode images and ROIs for inclusion DR calculation.

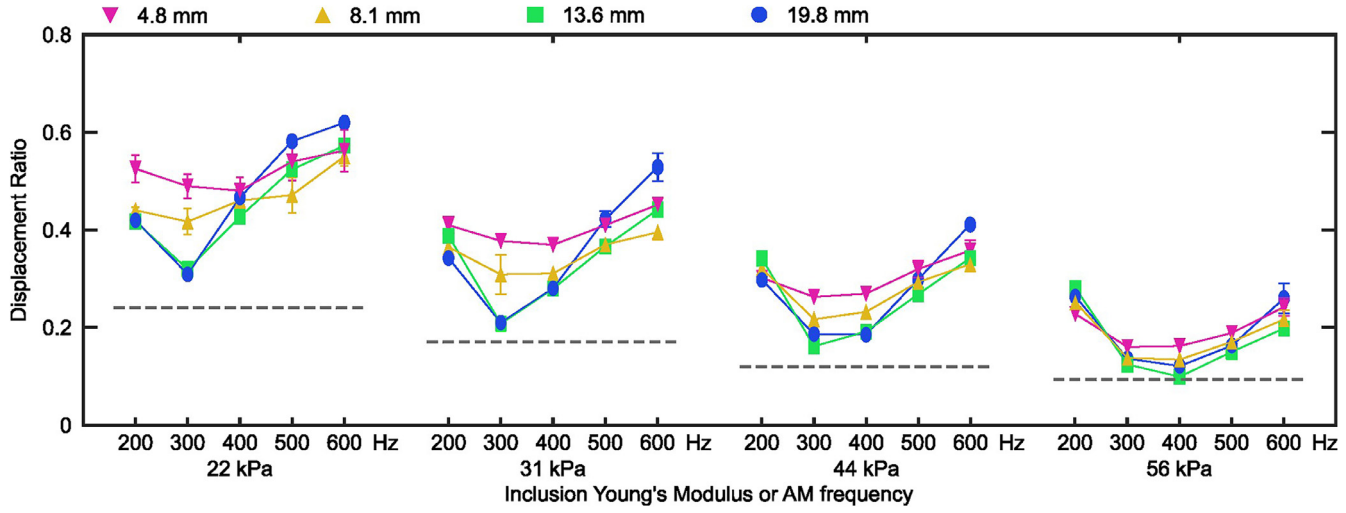

Figure 3. HMI-derived Inclusion DRs versus inclusion Young's moduli from 22 to 56 kPa (background Young's modulus: 5.3 kPa), applied AM frequencies from 200 to 600 Hz, and inclusion diameters from 4.8 to 19.8 mm. Data are plotted as mean ± one standard deviation over four independent measurements. Dashed gray lines indicate the Young's modulus ratio of the background to inclusions.

increases. Second, at some AM frequencies, e.g., 300 and 400 Hz, inclusion DRs decrease as the inclusion diameter increases; however, this phenomenon was not uniform across all AM frequencies. Third, for inclusions with a Young's modulus ≥ 44 kPa or a Young's modulus ratio to the background ≥ 8.3, 200 Hz produced consistent DRs (27.2% variation) across differently sized inclusions with the same Young's modulus. Last, for inclusions with a lower mechanical contrast (Young's modulus ≤ 31 kPa or Young's modulus ratio ≤ 5.8), 400 Hz was otherwise required to produce a similar DR for small (diameter: 4.8 mm) inclusions as those obtained at 200 Hz for larger counterparts. Since a single AM frequency of 200 Hz was not able to characterize mechanically low-contrast inclusions consistently and 400-Hz AM was recommended for small inclusions, Figure 4 demonstrates the application of multi-AM HMI in the 4.8-mm inclusions.

Figure 5 shows linear regressions between inverse DRs and Young's modulus ratios of the inclusion to background regardless of the inclusion

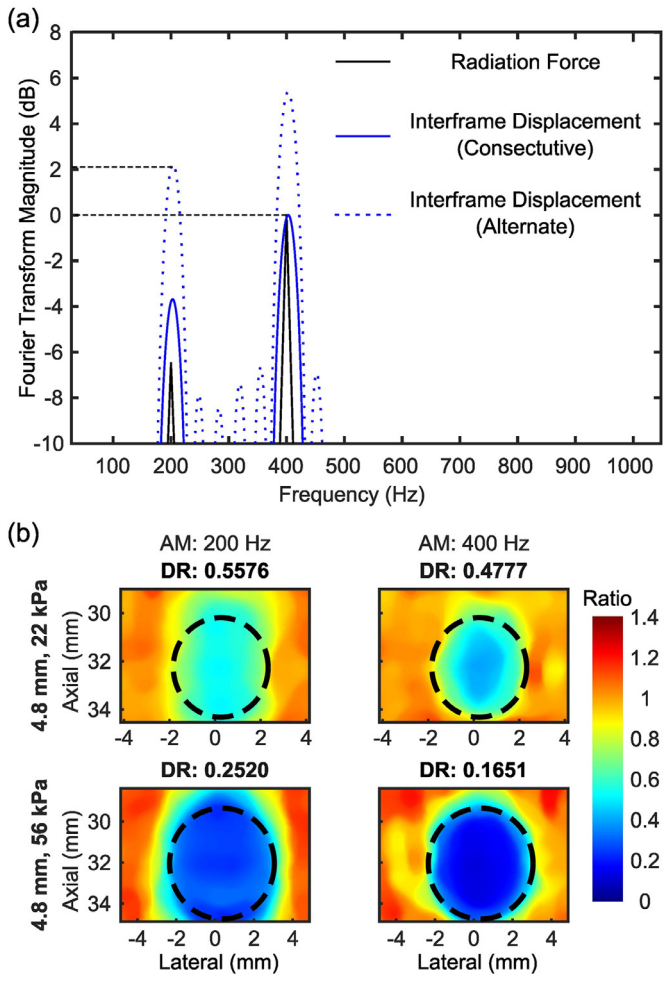

Figure 4. (a) Fourier transformations of the multi-AM excitation sequence, $\cos(2\pi * 200t) + 2\cos(2\pi * 400t)$, and estimated interframe displacements. Fourier transform magnitudes of the radiation force are normalized by that at 400 Hz and magnitudes of the interframe displacement are normalized by that at 400 Hz estimated between alternate frames. (b) Normalized HMI maps band-passed around individual AM frequencies (200 and 400 Hz). Dashed black contours represent the inclusion boundaries derived from the B-mode images.

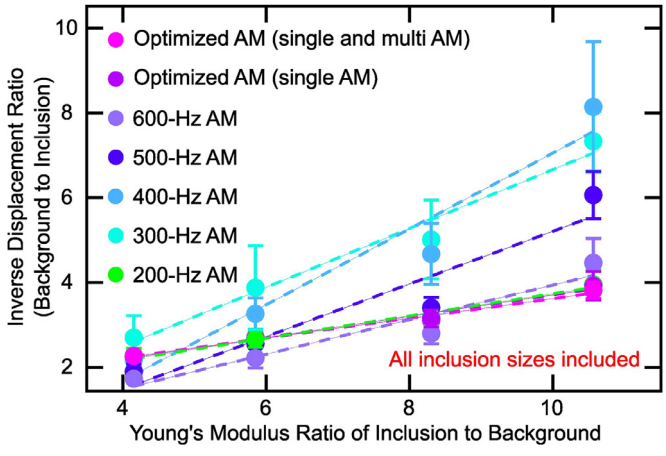

Figure 5. Linear regression between the inverse DR and Young's modulus ratio of the inclusion to background regardless of inclusion dimensions. Data are plotted as mean ± one standard deviation over 16 measurements (4 diameters and 4 independent measurements for each diameter).

Table 2
Slope, R2, and Root Mean Squared Error (RMSE) of Linear Regressions Between the Inverse DR and Young's Modulus Ratio of the Inclusion to Background

AM Frequency	Slope	R^2	RMSE (% slope)
200 Hz[a]	0.2613	0.8681	0.2497 (95.6%)
300 Hz[a]	0.6939	0.8042	0.8394 (121.0%)
400Hz[a]	**0.8941**	0.8233	1.0158 (113.6%)
500 Hz[a]	0.6203	0.8727	0.5807 (93.6%)
600 Hz[a]	0.4070	0.8376	0.4393 (107.9%)
Optimized, single-AM	0.2515	0.8770	0.2309 (91.8%)
Optimized, multi-AM	0.2329	**0.9043**	**0.1858 (79.8%)**

[a] Indicates statistically significant difference in the mean squared error (MSE) between optimized multi-AM and the corresponding group.
The highest slope, R2, and lowest RMSE are highlighted in bold. For better comparisons, the RMSE is also reported as a percentage of the corresponding slope.
Bold value indicates statistical significance at $p < 0.01$.

diameter. AM frequency optimization was done empirically based on which frequency produced the most consistent DRs across varying inclusion diameters. To summarize, 200 Hz was found optimal for large (≥8.1 mm) or stiff (≥44 kPa) inclusions, and 400 Hz was optimal for the rest cases (4.8 mm with a Young's modulus of either 22 or 31 kPa). Table 2 summarizes the slope, R^2, and RMSE of each regression. All linear regressions showed statistical significance, with 400 Hz having the highest slope. F-statistics suggested that MSE at the optimized frequency using multi-AM HMI was significantly lower than single AM frequencies. Meanwhile, 200 Hz had the lowest MSE ($p < 0.01$) among single AM frequencies.

Inclusion size estimation

Figure 6 shows inclusion size estimation using HMI for an 8.1-mm inclusion. Signed estimation errors over four independent measurements between the ground truth inclusion diameter derived from the B-mode images and estimated axial, lateral axes are plotted in Figure 7 for each AM frequency, inclusion diameter and Young's modulus. To correlate with the round inclusion shape, errors between the estimated equivalent diameter and ground truth are reported. Overall, 600 and 400 Hz produced the lowest axial and lateral axis estimation errors, respectively.

In vivo *clinical breast tumor imaging*

In Figure 8, four *in vivo* human malignant breast tumors (DCIS or IDC) were imaged using 200-Hz AM, considering their large dimensions (>10 mm). According to histopathology analysis of the excised breast tissues after the mastectomy, Patients 1 and 3 still had metastatic cancer cells post-NACT while Patient 2 achieved pathologic complete response (pCR), suggesting that no residual cancerous cells were found. Patient 4 had not completed NACT, and therefore no pathologic endpoints were reported. Due to respiratory motion and slight dragging of breast tissues between mechanical movements of the transducers, registered HMI maps of Patient 2, baseline (Fig. 8b), and Patient 4, 3-week follow-up (Fig. 8g) only included a limited area of surrounding healthy tissues. Despite that, tumor boundaries were successfully delineated and DRs of the tumor to surrounding noncancerous tissues were reported for all scans. The data acquisition duration was around 95 seconds for each scan. In Figure 9, an *in vivo* human benign breast tumor (fibroadenoma, Patient 5) with the largest dimension of around 10 mm was imaged using both multi-AM and single-AM HMI at 200 and 400 Hz for comparisons. The data acquisition duration was approximately 80 s.

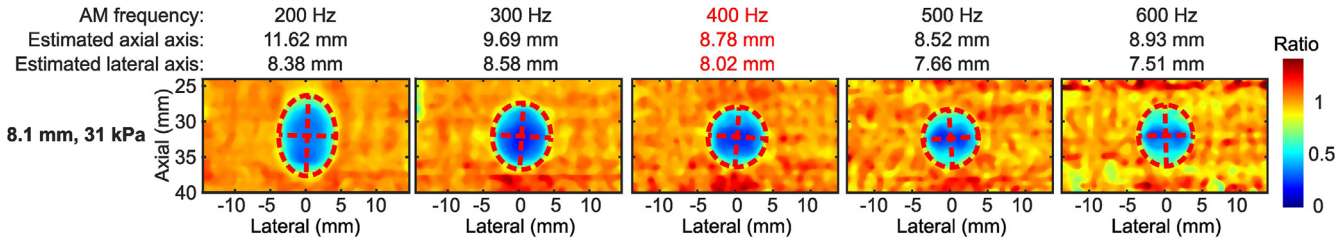

Figure 6. Examples of inclusion size estimation using HMI at different AM frequencies of an 8.1-mm and 31-kPa inclusion embedded in a 5.3-kPa background. Dashed red contours indicate the fitted ellipses and the axial and lateral axes. The most accurate overall estimations are highlighted in red.

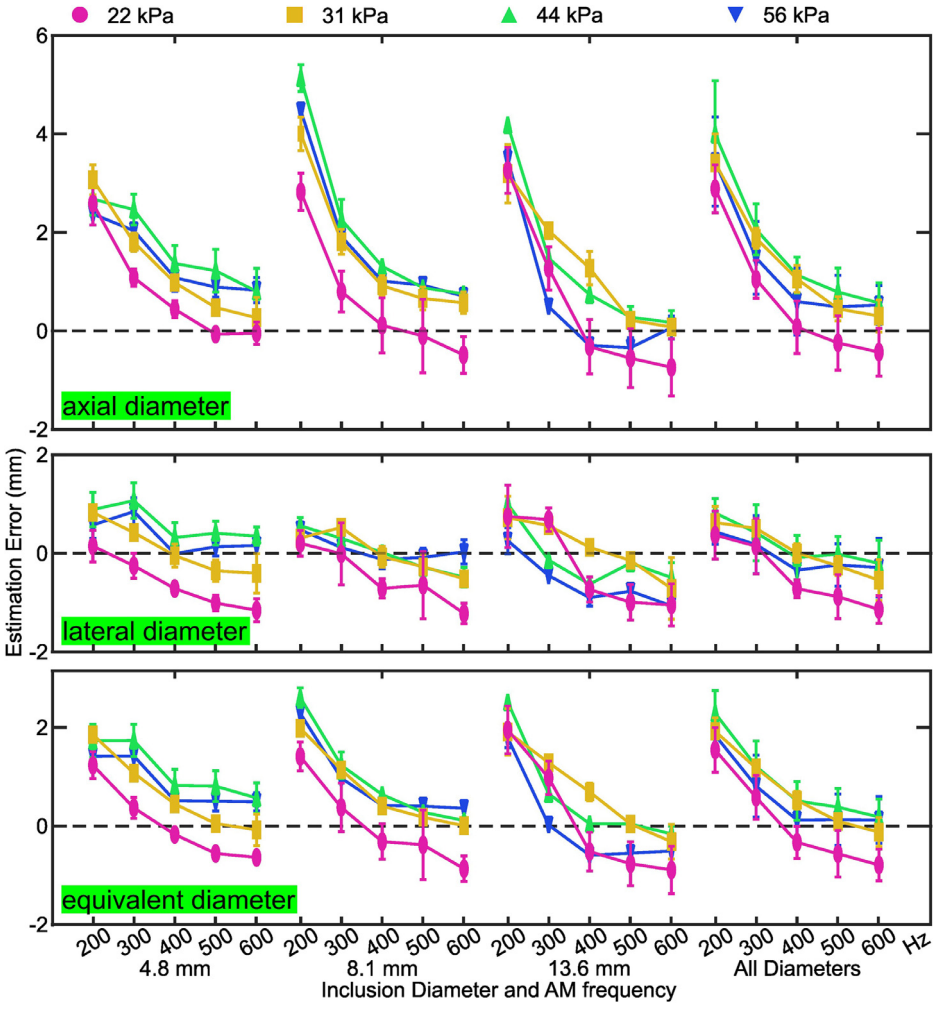

Figure 7. Inclusion size estimation errors using HMI between the estimated (top) axial, (mid) lateral axes, (bottom) equivalent diameter, and the ground truth diameter versus inclusion diameters (4.8 to 13.6 mm), applied AM frequencies (200 to 600 Hz), and inclusion Young's moduli (22 to 56 kPa, background: 5.3 kPa). Data are plotted as mean ± one standard deviation over four independent measurements.

Discussion

Characterization using ultrasound elastography can vary [4,37] among tumors with the same mechanical properties but different dimensions. Such underestimation of the inclusion stiffness and overestimation of the inclusion dimension may especially occur in cases of small inclusions and vice versa. This study sought to optimize the performance of HMI in imaging tumors of different dimensions, which is of primordial clinical significance in tumor characterization, response assessment to treatment, and surgical planning. First, the effects of the inclusion dimensions from 4.8 to 19.8 mm (n = 4) and AM frequencies from 200 to 600 Hz (n = 5) on the HMI DR measurement were studied in phantoms (background Young's modulus: 5.3 kPa) with cylindrical inclusions (22 to 56 kPa, n = 4). Properties of these inclusions were clinically relevant to breast tumors in terms of dimensions [4,38] and Young's moduli [4,42,46,47]. The goal was to obtain consistent HMI DRs for tumors with the same Young's modulus ratio to the background regardless of dimensions. Second, inclusion size estimation was evaluated at each AM frequency.

HMI-derived DRs of inclusions to the background serve as a surrogate measurement of relative stiffness. Figure 3 compares HMI DRs to the Young's modulus ratio (dashed gray lines) across a range of inclusion

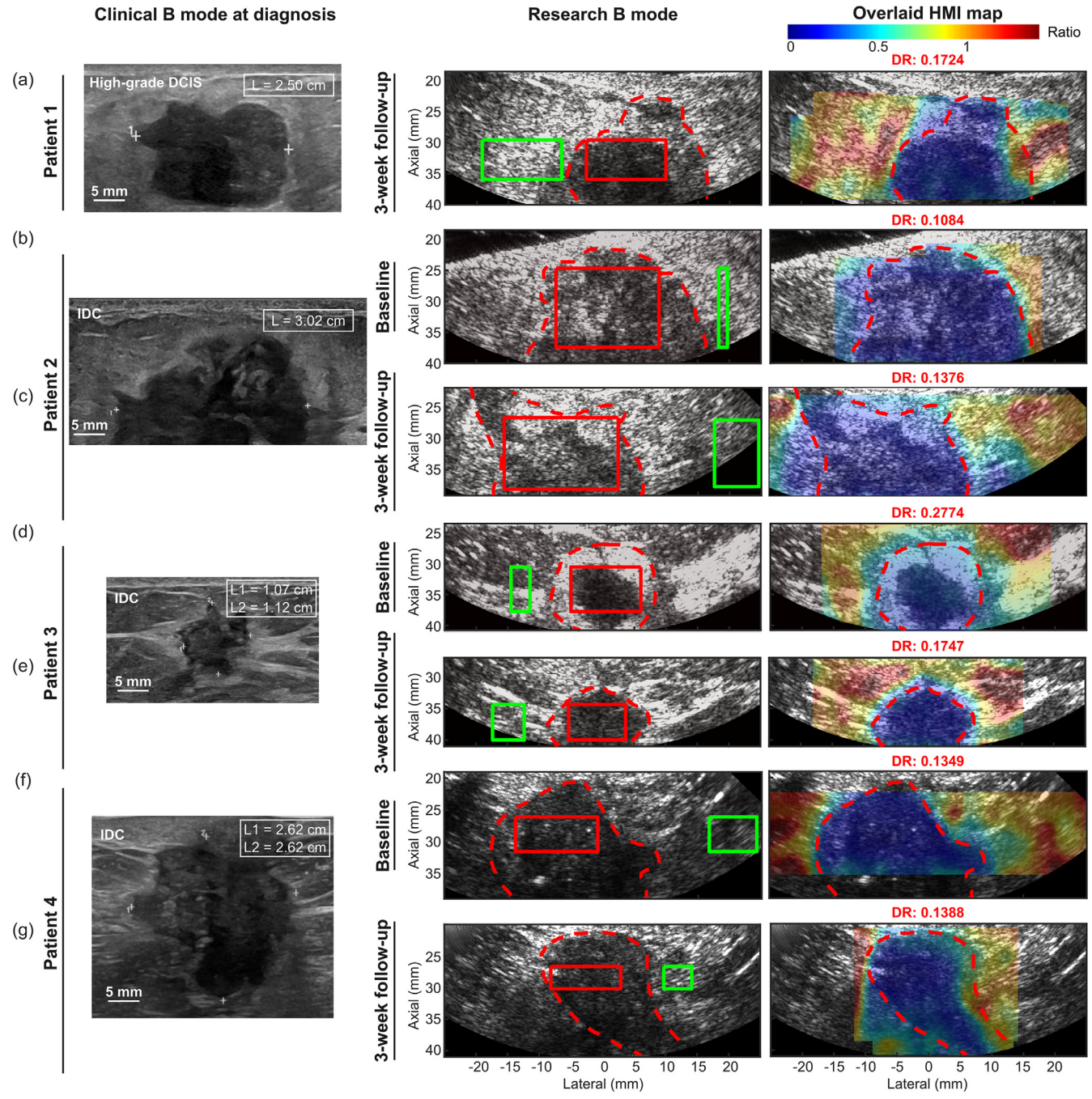

Figure 8. (Left) clinical B-mode, (mid) research B-mode, and (right) overlaid HMI maps (AM frequency: 200 Hz) of *in vivo* human malignant breast tumors (Patients 1–4). Serial HMI scans were performed at two different time-points over the course of neoadjuvant treatment. To note, baseline scans of Patient 1 were discarded due to technical issues. Dashed red, solid red and green contours represent the tumor boundaries derived from the B-mode images and ROIs for tumor DR calculation.

diameters and Young's moduli. In general, DRs was not equal to the Young's modulus ratio. In fact, according to the mass-spring-dashpot model, DRs not only depends on the shear modulus, but are also affected by the viscosity and inertia [21]. Rouze et al. [22] have shown such elastic phantoms were somewhat viscoelastic. Therefore, an inverse problem involving all these parameters should be considered to retrieve the modulus ratio from DRs, which is out of the scope of this study. Despite that, HMI DRs, measuring tissue relative stiffness, proved effective in characterizing breast [17,35] and pancreas [32] masses. To translate to clinical practice, ongoing preclinical and clinical studies, involving longitudinal scanning of breast cancer patients who are scheduled to receive neoadjuvant systemic treatment and HMI guided focused ultrasound thermal ablation, are being performed to establish a threshold or a look-up table for clinical interpretations. To retrieve the actual Young's modulus ratio, if necessary, a look-up table or DR-modulus ratio curve could be established.

For 22- and 31-kPa inclusions, 200-Hz AM produced agreeing DRs for inclusions with diameters ≥ 8.1 mm. However, DRs at 200 Hz of the 4.8-mm inclusions were 23.5 and 12.2% higher than their counterparts in greater dimensions, underestimating the relative stiffness. This was due to both the boundary effect, where reflections of generated shear waves interfere with the on-axis displacements, and the long shear wavelength, which averages displacements within and outside the inclusion [36,37,48]. These effects also contributed to the overestimated

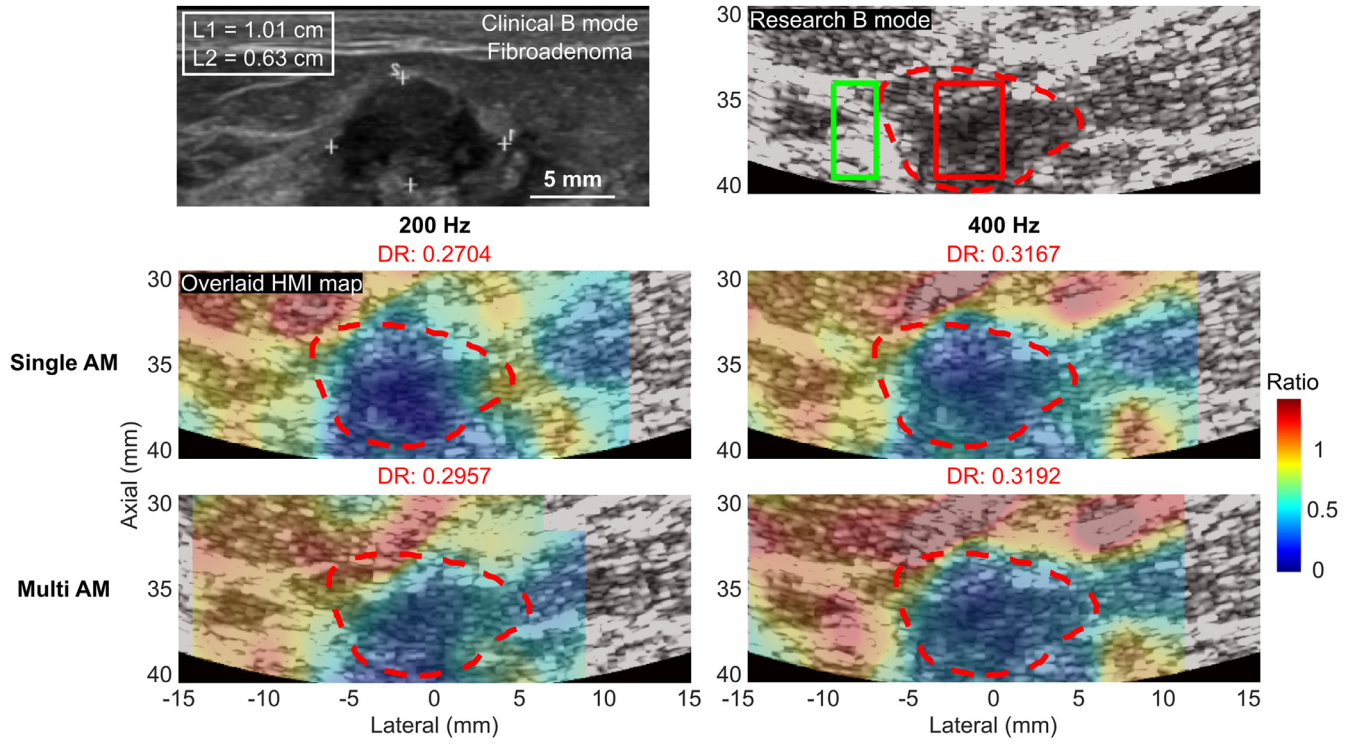

Figure 9. (Top left) clinical B-mode, (top right) research B-mode, and overlaid HMI maps from (mid) single-AM and (bottom) multi-AM HMI of an *in vivo* human benign breast tumor (Patient 5) diagnosed with fibroadenoma. Dashed red, solid red and green contours represent the tumor boundaries derived from the B-mode images and ROIs for tumor DR calculation. A slight axial shifting within 1 mm was observed between scans due to patient motions.

inclusion diameters as demonstrated in Figure 6 and Figure 7. In future studies, finite-element modeling and advanced filtering methods will be investigated to suppress the artifacts generated from shear wave interference. Nevertheless, a higher AM frequency of 400 Hz produced matching DRs for these inclusions. For highly contrast inclusions, i.e., 44 and 56 kPa, 200 Hz consistently produced DRs around 0.32 and 0.24 for all sizes from 4.8 to 19.8 mm. In summary, for inclusions with diameters $\geq$ 8.1 mm, 200 Hz was able to characterize the relative stiffness regardless of their dimensions. On the other hand, for smaller inclusions, 200 Hz was able to characterize the relative stiffness consistently if only the modulus ratio $\geq$ 8.3. These properties, i.e., greatest mass dimension $\geq$ 8.1 mm [4,38], Young's modulus $\geq$ 44 kPa [4,38,42], or modulus ratio $\geq$ 8.3 [4], were within the ranges in literature for clinical breast mass characterization. Furthermore, at high AM frequencies, i.e., 500 and 600 Hz, the shear wavelength is shorter, while the attenuation is higher compared to lower frequencies. Moreover, since the shear wave speed is lower for the 22-kPa than that of the 56-kPa inclusions, the wavelength shortens further. Consequently, as seen in Figure 2, increased variation in displacement estimation that averaged over a smaller region may be expected due to insufficient suppression of variations in displacements possibly resulting from inherent heterogeneity within the materials during manufacturing. Therefore, 200 Hz should be generally considered if multi-AM HMI cannot be implemented.

A multi-AM sequence consisting of 200 and 400 Hz was developed for imaging small lesions. In Figure 4b, HMI displacement maps from the multi-AM sequence were shown with comparable qualities as those from single-AM sequences in Figure 2. Meanwhile, DRs obtained from the multi-AM sequence were within the range of DRs from the single-AM sequences. This sequence was later demonstrated in *in vivo* human benign breast tumors in Figure 9. DRs of around 0.3 were obtained, much higher than the malignant cases in Figure 8, indicating a relatively softer lesion. In both single- and multi-AM HMI, 200 Hz overestimated the axial tumor dimensions, whereas 400 Hz did not exhibit this effect. Compared with single AM, multi-AM was more efficient since it produced HMI maps at various AM frequencies from a single data acquisition [36]. However, interactions between displacements at different frequencies should be investigated in future studies. Another limitation was that the generated acoustic radiation force was distributed to multiple AM frequencies, potentially decreasing the signal-to-noise ratio at individual frequencies. Higher FUS duty cycles will in the future be investigated towards compensation for this effect with careful safety precautions taken.

Linear regression fits were employed ($p < 0.01$) between the inverse DR and Young's modulus ratio of the inclusion to background regardless of the inclusion dimensions (Fig. 5). As summarized in Table 2, the highest slope of 0.8941 was achieved at 400 Hz, indicating the highest sensitivity in differentiating inclusions with different Young's moduli, albeit with a suboptimal RMSE for high-contrast inclusions (Fig. 5). The lowest RMSE ($p < 0.01$) and percent RMSE with respect to the slope, 0.1858 and 79.8%, were achieved at the optimized AM frequencies using multi-AM HMI, indicating the most consistent measurement of DR. Even though 200 Hz did not yield matching DRs for small (4.1-mm, 22-kPa) and large (8.1- to 19.8-mm, 22-kPa) inclusions, it gained an R^2 of 0.8681 with a relatively low percent RMSE, 95.6%. Moreover, the current setup allowed wider electronic beam steering ranges at lower frequencies (200 and 300 Hz), which rendered 200 Hz an optimal frequency for *in vivo* characterization of breast tumors. In addition, McGarry et al. have previously developed an analytical model of the displacement field induced by HMI [49]; a consistent and reliable measurement of DRs could aid in the implementation of this method for direct conversion from DRs to modulus ratios. Future work will focus on deriving the absolute lesion modulus using this method combining harmonic shear wave speed estimation in the background [48].

Overestimation of inclusion sizes was observed at low AM frequencies (Fig. 6), especially along the axial direction, forming an ellipsoidal shape. Notably, overestimation was more pronounced in stiffer inclusions (31 to 56 kPa vs. 22 kPa). This is because the shear wavelength is longer for stiffer materials. In addition, the ellipsoidal FUS excitation

focal spot (axial x lateral: 4.30 × 0. 39 mm) also contributed to the distorted delineation of inclusion shapes. Underestimation of the lateral dimension was otherwise observed at high AM frequencies, potentially due to the boundary effect, which depends on the AM frequency and inclusion configurations. Implementation of shear compounding [50] and modifications of the FUS focal spot using acoustic lens may compensate these effects. Alternatively, through the optimization of inclusion segmentation by manually or adaptively changing the thresholding value when using Otsu's method, the accuracy of inclusion size estimation could be further improved however subject to bias at individual frequencies. Due to phantom configurations, upper boundaries of the 19.8-mm inclusions were not identified on the B-mode images. Therefore, inclusion size estimation was not performed. As summarized in Figure 7, as the AM frequency increases, the extent of axial overestimation diminishes from ~3 mm at 200 Hz to 0-0.5 mm at 600 Hz. For lateral axis and equivalent diameter estimations, 400 Hz had the lowest estimation errors of ~0.5 mm and 0. Therefore, for tumor size estimation, 400-Hz AM provided the best trade-off. Future work will include automated *in vivo* tumor segmentation and size measurement using multifrequency HMI images and deep learning [51].

Since axial translation of the transducer assembly using the robotic arm were not enabled due to coupling issues, a Tx F-number of 4.1 [40] was used to obtain a wide imaging depth of field. Despite that, only part of the *in vivo* human tumors (Fig. 8 and Fig. 9) was captured axially due to the extensive volume, whereas lateral raster scanning was always adjusted to cover the entire tumor laterally. Interestingly, for Patient 2, the perceived lateral tumor dimensions were larger in HMI than B-mode, potentially due to the desmoplastic response [52] associated with malignant tumors. When calculating tumor DRs, ROIs were selected at the same depth in the background and inside the tumor. Furthermore, to quantify the tumor DR change over time, tumor DRs were calculated using the background displacements on the same side for each patient. Notably, due to patient positioning and bulk motion during data acquisition, only limited background was included in the final HMI maps (Fig. 8b, g). For both cases, a narrow background ROI was used for DR calculation. Ongoing work will aim to expand the HMI FOV. There were a 27% increase (Fig. 8b, c) and 37% decrease (Fig. 8d, e) in the tumor DRs, suggesting tumor softening and stiffening, respectively, three weeks after Patients 2 and 3 received their first doses of NACT infusions. These changes correlated with histopathology results and indicated that tumor softening at 3 weeks into NACT was associated with pCR while tumor stiffening could be indicative of nonresponders. Patient 1 had a relatively high tumor DR at the 3-week follow-up, indicating that her tumor was less stiff compared to other patients. However, she was not a complete responder according to the histopathology report; despite that, only micrometastasis was detected for this patient and clinical caliper measurements by the treating physician documented that the tumor dimension reduced from 3 to under 2 and 1 cm after six and nine weeks of treatment. These findings demonstrated the potential of HMI-derived DRs as an early biomarker for breast tumor response assessment. Tumor DRs of Patient 4, who had not completed the NACT, did not change appreciably at the 3-week follow-up. Therefore, she was not predicted to be a complete responder. Future work will focus on the correlation between tumor DRs and residual cancer burden [53].

In addition, the remaining limitations warrant additional investigation. First, the axial electronic beam steering range was -4 to 4 mm away from the FUS geometric focus. More drastic axial beam steering suffers from a significant decrease in the acoustic pressure *in situ*, compromising the displacement estimation SNR. To image deeper-seated (>3 cm) masses, axial steering up to at least 10 mm is required. Future studies will explore this capability of upgrading the system power supply to compensate the pressure loss. Other limitations were that only one background (5.3 kPa) and cylindrical inclusions were considered. Possibly, results may vary based on the inclusion geometry. Ongoing efforts are to design more complex elastic phantoms with various background properties and recruit more clinical patients.

Conclusions

The effects of AM frequencies and inclusion dimensions on inclusion characterization using HMI were investigated in terms of DR and size estimation. An elastic phantom with properties mimicking clinical breast tumors (background Young's modulus: 5.3 kPa, cylindrical inclusion Young's modulus: 22, 31, 44, 56 kPa, and diameter: 4.8, 8.1, 13.6, 19.8 mm) was imaged for this purpose. The 200-Hz AM frequency provided the best trade-off with the most consistent DR measurements for inclusions ≥8.1 mm, while a multi-AM sequence consisting of 200 and 400 Hz was developed for imaging smaller inclusions. Inverse DRs at the optimized AM frequencies were linearly correlated (R^2 = 0.9043) with Young's modulus ratios of the inclusion to background regardless of inclusion dimensions. The most accurate inclusion size estimation and most sensitive DR measurement were achieved using an AM frequency of 400 Hz. *In vivo* imaging of benign (n = 1) and malignant (n = 4) tumors in clinical breast cancer patients was performed at that frequency with the lowest estimation error. Findings indicated that HMI-derived DR at the optimized AM frequency of 200 Hz may be an informative biomarker for early assessment of tumor response to NACT.

Conflict of interest

The authors declare no conflicts of interest.

Data availability

All data associated with this study are available from the corresponding author on reasonable request.

Acknowledgments

This study was supported in part by the National Institutes of Health (R01CA228275). The authors would like to thank Niloufar Saharkhiz, Ph.D., for the insightful discussions, Julia E. McGuinness, M.D., Meghna S. Trivedi, M.D., Bret Taback, M.D., Shiqi Hu, M.S., Daniella A. Jimenez, B.S., Keyu Liu, B.S., for their assistance in the clinical study, and Pablo Abreu, M.A., for the administrative assistance.

References

[1] Siegel Mph RL, Miller KD, Sandeep N, Mbbs W, Ahmedin |, Dvm J, et al. Cancer statistics, 2023. CA Cancer J Clin 2023;73:17–48. doi: 10.3322/caac.21763.
[2] Keune JD, Jeffe DB, Schootman M, Hoffman A, Gillanders WE, Aft RL. Accuracy of ultrasonography and mammography in predicting pathologic response after neoadjuvant chemotherapy for breast cancer. Am J Surg 2010;199:477–84. doi: 10.1016/j.amjsurg.2009.03.012.
[3] Chagpar AB, Middleton LP, Sahin AA, Dempsey P, Buzdar AU, Mirza AN, et al. Accuracy of physical examination, ultrasonography, and mammography in predicting residual pathologic tumor size in patients treated with neoadjuvant chemotherapy. Ann Surg 2006;243:257–64. doi: 10.1097/01.sla.0000197714.14318.6f.
[4] Gu J, Polley EC, Denis M, Carter JM, Pruthi S, Gregory A V, et al. Early assessment of shear wave elastography parameters foresees the response to neoadjuvant chemotherapy in patients with invasive breast cancer. Breast Cancer Res 2021;23:52. doi: 10.1186/s13058-021-01429-4.
[5] Tai H, Margolis R, Li J, Hoyt K. H-scan ultrasound monitoring of breast cancer response to chemotherapy and validation with diffusion-weighted magnetic resonance imaging. J Ultrasound Med 2022;42(6):1297–306. doi: 10.1002/JUM.16143.
[6] Fernandes J, Sannachi L, Tran WT, Koven A, Watkins E, Hadizad F, et al. Monitoring breast cancer response to neoadjuvant chemotherapy using ultrasound strain elastography. Transl Oncol 2019;12:1177–84. doi: 10.1016/J.TRANON.2019.05.004.
[7] Li W, Newitt DC, Gibbs J, Wilmes LJ, Jones EF, Arasu VA, et al. Predicting breast cancer response to neoadjuvant treatment using multi-feature MRI: results from the I-SPY 2 TRIAL. Npj Breast Cancer 2020;6:1–6. doi: 10.1038/s41523-020-00203-7.
[8] Partridge SC, Zhang Z, Newitt DC, Gibbs JE, Chenevert TL, Rosen MA, et al. Diffusion-weighted MRI findings predict pathologic response in neoadjuvant treatment of breast cancer: the ACRIN 6698 multicenter trial. Radiology 2018;289:618–27. doi: 10.1148/RADIOL.2018180273/ASSET/IMAGES/LARGE/RADIOL.2018180273.FIG6.JPEG.
[9] Onishi N, Jones EF, Carmona-Bozo J, Gibbs JE, Bareng TJ, Molina-Vega J, et al. Abstract PD16-06: early MRI and PET biomarkers for hormone receptor-positive/HER2-negative early-stage breast cancer in the setting of neoadjuvant endocrine

therapy and neoadjuvant chemotherapy in the I-SPY 2 TRIAL. Cancer Res 2023;83:PD16–06. doi: 10.1158/1538-7445.SABCS22-PD16-06.
[10] Ophir J, Alam SK, Garra BS, Kallel F, Konofagou EE, Krouskop T, et al. Elastography: imaging the elastic properties of soft tissues with ultrasound. J Med Ultrason 2002;29:155–71. doi: 10.1007/bf02480847.
[11] Chen S, Sanchez W, Callstrom MR, Gorman B, Lewis JT, Sanderson SO, et al. Assessment of liver viscoelasticity by using shear waves induced by ultrasound radiation force. Radiology 2013;266:964–70. doi: 10.1148/RADIOL.12120837/-/DC1.
[12] Morris DC, Chan DY, Palmeri ML, Polascik TJ, Foo WC, Nightingale KR. Prostate cancer detection using 3-D shear wave elasticity imaging. Ultrasound Med Biol 2021;47:1670–80. doi: 10.1016/J.ULTRASMEDBIO.2021.02.006.
[13] Chan DY, Morris DC, Polascik TJ, Palmeri ML, Nightingale KR. Combined ARFI and shear wave imaging of prostate cancer: optimizing beam sequences and parameter reconstruction approaches. Ultrason Imaging 2023:175–86. doi: 10.1177/01617346231171895/ASSET/IMAGES/LARGE/10.1177_01617346231171895-FIG9.JPEG.
[14] Kawada N, Tanaka S, Uehara H, Ohkawa K, Yamai T, Takada R, et al. Potential use of point shear wave elastography for the pancreas: a single center prospective study. Eur J Radiol 2014;83:620–4. doi: 10.1016/J.EJRAD.2013.11.029.
[15] Bercoff J, Chaffai S, Tanter M, Sandrin L, Catheline S, Fink M, et al. In vivo breast tumor detection using transient elastography. Ultrasound Med Biol 2003;29:1387–96. doi: 10.1016/S0301-5629(03)00978-5.
[16] Kumar V, Denis M, Gregory A, Bayat M, Mehrmohammadi M, Fazzio R, et al. Viscoelastic parameters as discriminators of breast masses: initial human study results. PLoS One 2018;13:e0205717. doi: 10.1371/JOURNAL.PONE.0205717.
[17] Saharkhiz N, Lee SA, Li XJ, Konofagou EE. Pre-clinical breast cancer therapeutic response monitoring using harmonic motion imaging and functional ultrasound, 11. IEEE; 2021. p. 1–4.
[18] Nightingale K, Soo MS, Nightingale R, Trahey G. Acoustic radiation force impulse imaging: in vivo demonstration of clinical feasibility. Ultrasound Med Biol 2002;28:227–35. doi: 10.1016/S0301-5629(01)00499-9.
[19] Konofagou EE, Hynynen K. Localized harmonic motion imaging: theory, simulations and experiments. Ultrasound Med Biol 2003;29:1405–13. doi: 10.1016/S0301-5629(03)00953-0.
[20] Konofagou E, Hynynen K. Harmonic motion imaging: a new technique for the estimation of mechanical properties in tissues. Ultrasound Med Biol 2003;29:S59. doi: 10.1016/s0301-5629(03)00279-5.
[21] Hossain MM, Gallippi CM. Viscoelastic response ultrasound derived relative elasticity and relative viscosity reflect true elasticity and viscosity: in silico and experimental demonstration. IEEE Trans Ultrason Ferroelectr Freq Control 2020;67:1102–17. doi: 10.1109/TUFFC.2019.2962789.
[22] Rouze NC, Deng Y, Trutna CA, Palmeri ML, Nightingale KR. Characterization of viscoelastic materials using group shear wave speeds. IEEE Trans Ultrason Ferroelectr Freq Control 2018;65:780–94. doi: 10.1109/TUFFC.2018.2815505.
[23] Chen S, Fatemi M, Greenleaf JF. Quantifying elasticity and viscosity from measurement of shear wave speed dispersion. J Acoust Soc Am 2004;115:2781. doi: 10.1121/1.1739480.
[24] Ophir J, Cespedes I, Garra B, Ponnekanti H, Huang Y, Maklad N. Elastography: ultrasonic imaging of tissue strain and elastic modulus in vivo. Eur J Ultrasound 1996;3:49–70. doi: 10.1016/0929-8266(95)00134-4.
[25] Cho YS, Lim S, Kim Y, Kim TY, Jeong WK, Sohn JH. Abdominal wall thickness affects liver stiffness measurements by 2-D shear wave elastography in patients with chronic liver disease. Ultrasound Med Biol 2019;45:2697–703. doi: 10.1016/J.ULTRASMEDBIO.2019.06.415.
[26] Park SY, Choi JS, Han BK, Ko EY, Ko ES. Shear wave elastography in the diagnosis of breast non-mass lesions: factors associated with false negative and false positive results. Eur Radiol 2017;27:3788–98. doi: 10.1007/S00330-017-4763-6/FIGURES/3.
[27] Hollender PJ, Rosenzweig SJ, Nightingale KR, Trahey GE. Single- and multiple-track-location shear wave and acoustic radiation force impulse imaging: matched comparison of contrast, contrast-to-noise ratio and resolution. Ultrasound Med Biol 2015;41:1043–57. doi: 10.1016/j.ultrasmedbio.2014.11.006.
[28] Maleke C, Pernot M, Konofagou EE. Single-element focused ultrasound transducer method for harmonic motion imaging. Ultrason Imaging 2006;28:144–58. doi: 10.1177/016173460602800302.
[29] Hou GY, Provost J, Grondin J, Wang S, Marquet F, Bunting E, et al. Sparse matrix beamforming and image reconstruction for 2-D HIFU monitoring using harmonic motion imaging for focused ultrasound (HMIFU) with in vitro validation. IEEE Trans Med Imaging 2014;33:2107–17. doi: 10.1109/TMI.2014.2332184.
[30] Payen T, Palermo CF, Sastra SA, Chen H, Han Y, Olive KP, et al. Elasticity mapping of murine abdominal organs in vivo using harmonic motion imaging (HMI). Phys Med Biol 2016;61:5741–54. doi: 10.1088/0031-9155/61/15/5741.
[31] Hossain MM, Saharkhiz N, Konofagou EE. Feasibility of harmonic motion imaging using a single transducer: in vivo imaging of breast cancer in a Mouse Model and human subjects. IEEE Trans Med Imaging 2021;40:1390–404. doi: 10.1109/TMI.2021.3055779.
[32] Payen T, Oberstein PE, Saharkhiz N, Palermo CF, Sastra SA, Han Y, et al. Harmonic motion imaging of pancreatic tumor stiffness indicates disease state and treatment response. Clin Cancer Res 2020;26:1297–308. doi: 10.1158/1078-0432.CCR-18-3669/74159/AM/HARMONIC-MOTION-IMAGING-OF-PANCREATIC-TUMOR.
[33] Nabavizadeh A, Payen T, Iuga AC, Sagalovskiy IR, Desrouilleres D, Saharkhiz N, et al. Noninvasive Young's modulus visualization of fibrosis progression and delineation of pancreatic ductal adenocarcinoma (PDAC) tumors using Harmonic Motion Elastography (HME) in vivo. Theranostics 2020;10:4614–26. doi: 10.7150/THNO.37965.
[34] Han Y, Wang S, Hibshoosh H, Taback B, Konofagou E. Tumor characterization and treatment monitoring of postsurgical human breast specimens using harmonic motion imaging (HMI). Breast Cancer Res 2016;18:1–11. doi: 10.1186/S13058-016-0707-3/FIGURES/5.
[35] Saharkhiz N, Ha R, Taback B, Li XJ, Weber R, Nabavizadeh A, et al. Harmonic motion imaging of human breast masses: an in vivo clinical feasibility. Sci Rep 2020;10:15254. doi: 10.1038/s41598-020-71960-5.
[36] Hossain MM, Konofagou EE. Imaging of single transducer-harmonic motion imaging-derived displacements at several oscillation frequencies simultaneously. IEEE Trans Med Imag 2022;2022:3099–115. doi: 10.1109/TMI.2022.3178897.
[37] Saharkhiz N, Kamimura HAS, Konofagou EE. The impact of amplitude modulation frequency in harmonic motion imaging on inclusion characterization. Ultrasound Med Biol 2023;49:1768–79. doi: 10.1016/j.ultrasmedbio.2023.03.025.
[38] Denis M, Gregory A, Bayat M, Fazzio RT, Whaley DH, Ghosh K, et al. Correlating tumor stiffness with immunohistochemical subtypes of breast cancers: prognostic value of comb-push ultrasound shear elastography for differentiating luminal subtypes. PLoS One 2016;11:e0165003. doi: 10.1371/JOURNAL.PONE.0165003.
[39] Saharkhiz N, Kamimura HAS, Konofagou EE. An efficient and multi-focal focused ultrasound technique for harmonic motion imaging. IEEE Trans Biomed Eng 2022;70:1–12. doi: 10.1109/TBME.2022.3211465.
[40] Liu Y, Saharkhiz N, Hossain MM, Konofagou EE. Optimization of the tracking beam sequence in Harmonic Motion Imaging. IEEE Trans Ultrason Ferroelectr Freq Control 2023. doi: 10.1109/TUFFC.2023.3329729.
[41] Urban MW, Greenleaf JF. A Kramers–Kronig-based quality factor for shear wave propagation in soft tissue. Phys Med Biol 2009;54(19):5919. doi: 10.1088/0031-9155/54/19/017.
[42] Gu J, Polley EC, Boughey JC, Fazzio RT, Fatemi M, Alizad A. Prediction of invasive breast cancer using mass characteristic frequency and elasticity in correlation with prognostic histologic features and immunohistochemical biomarkers. Ultrasound Med Biol 2021;47:2193–201. doi: 10.1016/J.ULTRASMEDBIO.2021.03.039.
[43] Luo J, Konofagou E. A fast normalized cross-correlation calculation method for motion estimation. IEEE Trans Ultrason Ferroelectr Freq Control 2010;57:1347–57. doi: 10.1109/TUFFC.2010.1554.
[44] de Jong PGM, Arts T, Hoeks APG, Reneman RS. Determination of tissue motion velocity by correlation interpolation of pulsed ultrasonic echo signals. Ultrason Imag 1990;12:84–98. doi: 10.1177/016173469001200202.
[45] Gal O. https://www.mathworks.com/matlabcentral/fileexchange/3215-fit_ellipse. MATLAB Central File Exchange 2003. Retrieved August 1, 2023.
[46] Goenezen S, Dord JF, Sink Z, Barbone PE, Jiang J, Hall TJ, et al. Linear and nonlinear elastic modulus imaging: an application to breast cancer diagnosis. IEEE Trans Med Imaging 2012;31:1628–37. doi: 10.1109/TMI.2012.2201497.
[47] Bernal M, Chammings F, Couade M, Bercoff J, Tanter M, Gennisson JL. In vivo quantification of the nonlinear shear modulus in breast lesions: feasibility study. IEEE Trans Ultrason Ferroelectr Freq Control 2016;63:101–9. doi: 10.1109/TUFFC.2015.2503601.
[48] Hossain MM, Konofagou EE. Feasibility of phase velocity imaging using multi frequency oscillation-shear wave elastography. IEEE Trans Biomed Eng 2023;71:1–14. doi: 10.1109/TBME.2023.3309996.
[49] McGarry MDJ, Campo A, Payen T, Han Y, Konofagou EE. An analytical model of full-field displacement and strain induced by amplitude-modulated focused ultrasound in harmonic motion imaging. Phys Med Biol 2021;66:075017. doi: 10.1088/1361-6560/ABDDD1.
[50] Song P, Manduca A, Zhao H, Urban MW, Greenleaf JF, Chen S. Fast shear compounding using robust 2-D shear wave speed calculation and multi-directional filtering. Ultrasound Med Biol 2014;40:1343–55. doi: 10.1016/J.ULTRASMEDBIO.2013.12.026.
[51] Hu S, Hossain MM, Li X, Konofagou EE. Lesion size assessment on multi-frequency single transducer-harmonic motion imaging using convolutional neural network, 18. IEEE; 2023 Apr. p. 1–4.
[52] Insana MF, Pellot-Barakat C, Sridhar M, Lindfors KK. Viscoelastic imaging of breast tumor microenvironment with ultrasound. J Mammary Gland Biol Neoplasia 2004;9:393–404. doi: 10.1007/S10911-004-1409-5/METRICS.
[53] Symmans WF, Wei C, Gould R, Yu X, Zhang Y, Liu M, et al. Long-term prognostic risk after neoadjuvant chemotherapy associated with residual cancer burden and breast cancer subtype. J Clin Oncol 2017;35:1049. doi: 10.1200/JCO.2015.63.1010.